

# A Multitechnique Study of CO Adsorption on the TiO<sub>2</sub> Anatase (101) Surface

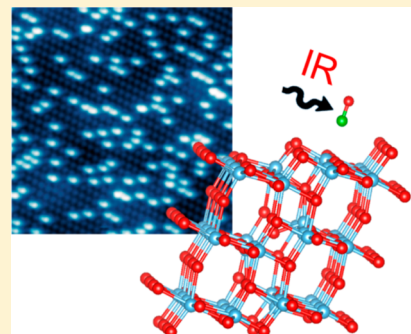
Martin Setvin,<sup>\*,†</sup> Maria Buchholz,<sup>‡</sup> Weiyi Hou,<sup>§</sup> Cui Zhang,<sup>§</sup> Bernhard Stöger,<sup>†</sup> Jan Hulva,<sup>†</sup> Thomas Simschitz,<sup>†</sup> Xiao Shi,<sup>§</sup> Jiri Pavleček,<sup>†</sup> Gareth S. Parkinson,<sup>†</sup> Mingchun Xu,<sup>‡</sup> Yuemin Wang,<sup>‡</sup> Michael Schmid,<sup>†</sup> Christof Wöll,<sup>‡</sup> Annabella Selloni,<sup>§</sup> and Ulrike Diebold<sup>†</sup>

<sup>†</sup>Institute of Applied Physics, TU Wien, Wiedner Hauptstrasse 8-10/134, 1040 Vienna, Austria

<sup>‡</sup>Institute of Functional Interfaces, Karlsruhe Institute of Technology, 76021 Karlsruhe, Germany

<sup>§</sup>Department of Chemistry, Princeton University, Frick Laboratory, Princeton, New Jersey 08544, United States

**ABSTRACT:** The adsorption of carbon monoxide on the anatase TiO<sub>2</sub> (101) surface was studied with infrared reflection absorption spectroscopy (IRRAS), temperature-programmed desorption (TPD), X-ray photoelectron spectroscopy (XPS), scanning tunneling microscopy (STM), and density functional theory (DFT). The IRRAS data reveal only one CO band at  $\sim 2181\text{ cm}^{-1}$  for both stoichiometric and reduced TiO<sub>2</sub> (101) surfaces. From TPD, an adsorption energy of  $0.37 \pm 0.03\text{ eV}$  is estimated for the isolated molecule, which shifts to slightly smaller values at higher coverages. Combining STM imaging and controlled annealing of the sample confirms the adsorption energies estimated from TPD and the slight repulsive intermolecular interaction. CO molecules desorb from electron-rich, extrinsic donor defect sites at somewhat higher temperatures. Confronting the experimental results with DFT calculations indicates that the anatase (101) surface does not contain any significant concentration of subsurface oxygen vacancies in the near-surface region. Comparison with CO adsorption on the rutile TiO<sub>2</sub> (110) surface shows that the tendency for excess electron localization in anatase is much weaker than in rutile.



## INTRODUCTION

TiO<sub>2</sub> is a prototypical material used in catalysis,<sup>1,2</sup> photocatalysis,<sup>3</sup> and Grätzel solar cells.<sup>4</sup> It also has promising properties for use in electronics as a transparent conductive oxide<sup>5,6</sup> or a memristor.<sup>7</sup> TiO<sub>2</sub> has two main polymorphs relevant in industry: rutile and anatase.<sup>8</sup> Rutile has been the subject of numerous works in surface science.<sup>8</sup> In contrast, relatively little is known about the metastable anatase, which is preferably used in most applications.

CO adsorption is an important process in heterogeneous catalysis. TiO<sub>2</sub> is used in various catalytic reactions including low-temperature CO oxidation,<sup>9</sup> CO hydrogenation,<sup>10</sup> the water gas shift reaction,<sup>11</sup> and the oxidation of CO by NO.<sup>12</sup> CO binds with its C atom to 5-fold coordinated surface Ti atoms (Ti<sub>5c</sub>) upon adsorption on TiO<sub>2</sub>.<sup>13–16</sup> CO adsorption on the prototypical rutile TiO<sub>2</sub> (110) has been studied in detail by various methods. On a stoichiometric rutile (110) surface, temperature-programmed desorption (TPD)<sup>17–19</sup> shows a CO desorption peak at  $\sim 145\text{ K}$  (corresponding to  $E_{\text{ads}1} = 0.38\text{ eV}$ ). The peak broadens at higher CO coverages, which was attributed to CO–CO repulsions in the layer and a decrease of the adsorption energy down to  $0.20\text{ eV}$  in a 1 ML coverage limit.<sup>19</sup> After the surface was reduced, a shoulder was observed at a higher temperature of  $\sim 170\text{ K}$ , corresponding to an  $E_{\text{ads}2} = 0.44\text{ eV}$ .<sup>17</sup> In infrared (IR) spectroscopy a single adsorption peak<sup>20</sup> at  $2188\text{ cm}^{-1}$  is observed for CO adsorbed on a

stoichiometric rutile (110) surface. After reduction, a secondary peak evolved at  $2178\text{ cm}^{-1}$ . The increase in the CO adsorption energy and the secondary peak in the IR absorption spectra are related to surface oxygen vacancies ( $V_{\text{OS}}$ ) present at the reduced surface and to excess electrons donated to the material.<sup>15</sup>

Infrared reflection absorption spectroscopy (IRRAS) studies of CO adsorption on anatase are mostly limited to powders;<sup>21–23</sup> only one work reported measurements on a single crystal.<sup>24</sup> In contrast to rutile (110), anatase (101) does not contain any surface  $V_{\text{OS}}$ .<sup>25,26</sup> It has been shown that artificially created  $V_{\text{OS}}$  migrate subsurface below room temperature, but further involvement of such subsurface species in the material's surface chemistry remains an open issue. A recent density functional theory (DFT) study<sup>27</sup> has predicted that adsorption above subsurface  $V_{\text{OS}}$  (second subsurface layer) should result in a significant redshift of  $20\text{ cm}^{-1}$  compared to regular Ti<sub>5c</sub> sites. This offers a method for probing the concentration of subsurface  $V_{\text{OS}}$ . The present study, which combines IR with TPD, X-ray photoelectron spectroscopy (XPS), and scanning tunneling microscopy (STM), is partially motivated by this result. While our DFT calculations confirm

Received: August 17, 2015

Revised: August 23, 2015

Published: August 24, 2015

that near-surface V<sub>OS</sub>s should show a significant shift of the CO stretching frequency, and concurrent increase in binding energy, this is not borne out by the experimental data. We conclude that subsurface V<sub>OS</sub>s are not a major player in the adsorption of CO and that the differences in the desorption behavior of rutile and anatase are mainly due to the different nature of excess electrons, i.e., polaronic versus delocalized character.

## ■ EXPERIMENTAL AND THEORETICAL METHODS

The experiments were performed in three separate ultrahigh vacuum (UHV) chambers. In each case, anatase mineral samples were used as specimen, and the preparation procedure described in ref 28 was followed.

The IRRAS measurements were performed in a UHV Fourier transform infrared spectroscopy (FTIRS) combination system.<sup>29</sup> In addition to a state-of-the-art vacuum FTIR spectrometer, the apparatus contains also a separate analysis chamber with XPS and ultraviolet photoelectron spectroscopy (UPS) as well as distribution and measurement chambers. The sample temperature could be varied between 50 K (He flow cryostat) and 900 K by resistive heating. Each IR spectrum was accumulated in 2048 scans with a resolution of 2 cm<sup>-1</sup> and was taken at grazing incidence (80°) at a base pressure of 7 × 10<sup>-11</sup> mbar. The optical path inside the IR spectrometer and the space between the spectrometer and UHV chamber were kept under vacuum to avoid any unwanted IR adsorption from gas-phase species. The single crystal used in the IRRAS measurements had a size of 5 × 5 mm<sup>2</sup> (MaTeck, Jülich, Germany). Preparation was considered successful when a high-quality (1 × 1) low-energy electron diffraction (LEED) pattern was observed. The cleanliness of the sample was further checked by XPS. CO gas with a purity of 99.98% was used. The CO was dosed at 70 K, and the dosing pressure was set in order to keep the dosing time in the range of 30–120 s. The IRRAS spectra were taken directly after the exposure. Exposures are given in langmuir (1 langmuir = 1.33 × 10<sup>-6</sup> mbar s). All IRRAS spectra were obtained by subtracting a background recorded immediately before exposure to CO.

The TPD measurements were performed in a separate UHV system with a base pressure of 5 × 10<sup>-11</sup> mbar using a HIDEN quadrupole mass spectrometer in a line-of-sight configuration. Here the anatase sample was mounted on a Ta back plate, cooled by a Janis ST-400 UHV liquid-He flow cryostat, and heated by direct current through the back plate. The temperature was measured by a K-type thermocouple spot-welded to the sample plate and calibrated using multilayer desorption of several gases (O<sub>2</sub>, H<sub>2</sub>O, CO). The resulting uncertainty in the absolute temperature reading is estimated to be ±3 K (increasing up to ±10 K at very low temperatures below ~40 K). During the TPD measurements, the sample was biased at -100 V to prevent electrons from the filament reaching the sample surface. CO was dosed by an effusive molecular beam with a top-hat profile, formed by expanding 0.1–0.4 Torr through a circular orifice of diameter 50 μm. This produces a beam spot of ≈3.5 mm diameter at the sample. The dose rate under these conditions is approximately 1.2 ML/min. Only the TiO<sub>2</sub> sample surface is exposed to the CO beam. For the TPD measurements, a linear temperature ramp of 1 K/s was used.

XPS spectra were measured in the same vacuum system with a hemispherical electrostatic energy analyzer (SPECS Phoibos 150), using a monochromatized Al Kα X-ray source (SPECS

Focus 500). Data were recorded at a sample temperature of  $T = 34$  K. Any influence of the X-rays and contamination from the residual gas was carefully checked by TPD spectra recorded after the XPS data were taken; no radiation-induced damage was observed.

STM measurements were performed at  $T = 78$  K in a third UHV chamber with a base pressure below  $1 \times 10^{-11}$  mbar, equipped with a commercial Omicron LT-STM head. Electrochemically etched W STM tips were cleaned by Ar<sup>+</sup> sputtering and treated on a Au (110) surface to obtain a reproducible, metallic tip condition. Low-temperature sample annealing was performed in a manipulator cooled by flowing nitrogen gas. The temperature was measured by a K-type thermocouple attached to the sample holder. We estimate that the quoted temperatures are accurate within ±10 K. Single-crystalline mineral anatase TiO<sub>2</sub>(101) surfaces were prepared by ex-situ cleaving or polishing (both types were used) and subsequent cleaning in vacuum by cycles of Ar<sup>+</sup> sputtering (1 keV) and annealing to 950 K.<sup>28</sup>

CO adsorption on stoichiometric and reduced anatase (101) was investigated by DFT-PBE, as implemented in the Quantum-ESPRESSO package.<sup>30</sup> This approach has been used and found to work well in previous studies of water<sup>31</sup> and O<sub>2</sub> adsorption<sup>32</sup> on anatase (101). Calculations using the Grimme D2<sup>33</sup> dispersion corrections were also performed for a few cases (see below). We used ultrasoft pseudopotentials<sup>34</sup> with plane-wave kinetic-energy cutoffs of 35 and 350 Ry for the smooth part of the electronic wave functions and augmented charge density, respectively. Vibrational properties were determined using both the linear response method<sup>30</sup> and a finite difference approach, in which a partial Hessian matrix was built by displacing only the CO nuclei by 0.005 Å in both directions of each Cartesian coordinate. The latter approach is less precise but allows us to consider rather large systems, which are cumbersome to treat with linear response.

The anatase (101) surface was modeled with periodically repeated slabs separated by a 16 Å wide vacuum layer with two different setups. In the finite-difference calculations we used a slab model of three TiO<sub>2</sub> trilayers and (1 × 4) surface supercells with an area of 10.21 × 15.10 Å<sup>2</sup>, corresponding to a total of 48 Ti and 96 O atoms per unit cell. The reduced surface was modeled by introducing one subsurface oxygen vacancy in the second layer of the slab. In the linear response calculations, we used a slab of two TiO<sub>2</sub> trilayers and (1 × 2) surface supercells with an area of 10.21 × 7.60 Å<sup>2</sup>, corresponding to a total of 16 Ti and 32 O atoms per unit cell. In this case, the reduced surface was modeled by adsorbing two H atoms on bridging oxygen sites of the bottom surface. The CO adsorption energies on the two different slab geometries agree within 8 meV (first four lines of Table 1). In the geometric optimizations, all atoms were relaxed until the residual forces were smaller than 0.03 eV/Å.

## ■ RESULTS

**Infrared Absorption Spectroscopy.** The IRRAS results are shown in Figure 1. For the spectra displayed in the top panel (Figure 1a), a sample was used where the XPS measurements of the Ti 2p peak showed absence of the Ti<sup>3+</sup> shoulder;<sup>8</sup> we conclude a low reduction state of the sample. Figure 1a displays the IRRAS spectra of CO adsorption at 95 K. At low coverage, a single peak at 2185 cm<sup>-1</sup> was detected for the CO stretching frequency (Figure 1a). Upon increasing the CO coverage close to 1 monolayer (ML), the peak exhibits a

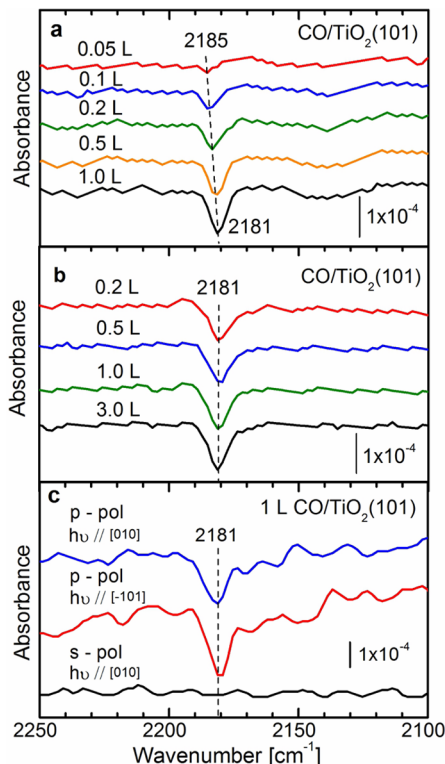


**Figure 1.** IRRAS data of different doses of CO adsorbed at 95 K on (a) stoichiometric and (b) reduced anatase (101) surfaces with nonpolarized light; (c) IRRAS data of 1 L CO adsorbed at 70 K on stoichiometric  $\text{TiO}_2(101)$  with p-polarized light along  $[010]$  and  $[-101]$  and s-polarized light along the  $[010]$  azimuth.

slight redshift to  $2181 \text{ cm}^{-1}$ . Figure 1c shows the IR data measured with p- and s-polarized light. With p-polarized light, only a negative CO band at  $2181 \text{ cm}^{-1}$  was observed, indicating that the dynamic dipole moment of the CO stretch vibration interacts mainly with the component of the p-polarized light normal to the surface.<sup>29</sup> No substantial difference was observed between light incident along the  $[010]$  and the  $[-101]$  direction (see Figure 1c). No vibrational band was visible with s-polarized light (Figure 1c). The s-polarized light is oriented parallel to the surface and perpendicular to the incidence direction. This indicates that the CO adopts an orientation nearly perpendicular to the surface.

IRRAS data of samples subjected to many sputter-annealing cycles (a procedure known to reduce the surface) also show a single CO band at  $2181 \text{ cm}^{-1}$  (Figure 1b). This behavior is different from the case of rutile  $\text{TiO}_2(110)$ <sup>20</sup> or  $\text{CeO}_2(111)$ ,<sup>35</sup> where surface reduction resulted in the appearance of a secondary CO-stretching peak red-shifted by  $\sim 10 \text{ cm}^{-1}$  compared to the vibrational band observed on the stoichiometric surface. On anatase  $\text{TiO}_2(101)$ , distinct additional peaks were not detected (see Figure 1b). The measurements were repeated several times on two different anatase mineral samples, with very similar results.

**Temperature-Programmed Desorption.** The desorption of CO adsorbed on a stoichiometric anatase (101) was studied by TPD, see Figure 2. The submonolayer regime is dominated by a peak that emerges at 135 K and shifts to 118 K with increasing coverage. The peak exhibits a small tail above 140 K, most likely associated with desorption from the vicinity of subsurface defects (see STM results, below). Following

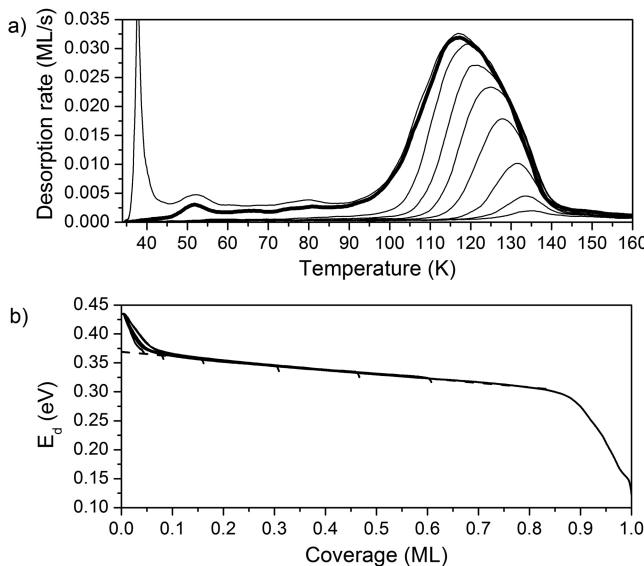


**Figure 2.** (a) TPD spectra of CO adsorbed on the anatase (101) surface for coverages ranging from 0.07 to 1.2 ML (1.2, 1.0 (bold), 0.79, 0.63, 0.49, 0.34, 0.19, 0.11, and 0.07 ML); (b) desorption energy as a function of coverage obtained by direct inversion of the Polanyi–Wigner equation (see text). Extrapolation of the linear regime to zero coverage suggests a binding energy for the isolated molecule of 0.37 eV.

saturation of the main peak, two small peaks emerge at 80 and 53 K before desorption from multilayers begins at 37 K. A discussion of the origin of these peaks goes beyond the scope of this paper; possibly they are related to special sites such as defects or step edges. The coverages were calculated by integrating the area under each curve and normalizing to the spectrum obtained immediately prior to the onset of multilayer desorption (thick line in Figure 2a). The kinetic parameters were extracted by direct inversion of the Polanyi–Wigner equation assuming the pre-exponential factor ( $\nu$ ) to be independent of coverage ( $\theta$ ) and the desorption order to be unity, following the method described in detail in ref 36. The desorption energy for each spectrum is calculated as<sup>36</sup>

$$E_d(\theta) = -kT \ln\left(\frac{-d\theta/dT}{\beta\nu\theta}\right) \quad (1)$$

where  $k$  is the Boltzmann constant,  $T$  the temperature, and  $\beta$  the heating rate (1 K/s). In eq 1, all parameters are known except for  $\nu$ , which is treated as a parameter. When the procedure from ref 36 was followed, the appropriate value was found by ensuring that curves overlay for different initial coverages. This was the case for pre-exponential factors of  $10^{13 \pm 1} \text{ s}^{-1}$ . Shown in Figure 2b are  $E_d(\theta)$  curves calculated from the TPD data in Figure 2a using  $\nu = 10^{13} \text{ s}^{-1}$ . Varying the pre-exponential factor by 1 order of magnitude shifts the curves by  $\pm 0.03 \text{ eV}$ ; we use this value as an estimate of our experimental error.

The coverage-dependent desorption energies in Figure 2b show three distinct regions. For very low coverages ( $< 0.1 \text{ ML}$ ), the curves point upward, indicating higher binding energies. In agreement with the STM result (see below) this is attributed to adsorption near donor sites. Note, however, that the finite pumping speed in TPD experiments can cause high-temperature tails in TPD peaks. This affects the low-coverage region as well, rendering the analysis less reliable (the curves obtained for

different initial coverages do not perfectly overlap in the lowest coverage regime). In the range of 0.1–0.85 ML, the desorption energy shows a linear behavior and decreases slightly with coverage. A similar behavior was observed for CO on stoichiometric rutile  $\text{TiO}_2(110)$  and is attributed to intermolecular repulsion destabilizing the monolayer,<sup>18</sup> although the effect is much smaller in the present case on anatase. An extrapolation to zero coverage (dotted line) allows an estimate of 0.37 eV for the desorption energy of an isolated molecule (“singleton”<sup>37</sup>) on a perfect surface. The coverage of 0.85 ML (estimated from TPD by the procedure described above) corresponds to the situation in which all  $\text{Ti}_{\text{sc}}$  sites at the terraces are occupied by CO molecules (see STM results below). The adsorption energy at this point is 0.31 eV. The decrease in binding energy for very high coverages (>0.85 ML) in Figure 2b corresponds to desorption from lower-temperature states.

**STM Measurements.** STM was used to obtain local information about the CO adsorption configurations. We performed an experiment mimicking the TPD experiment, albeit with a much longer time constant. A full monolayer of CO was dosed at 78 K, which saturates (almost) all surface  $\text{Ti}_{\text{sc}}$  sites (Figure 3a).<sup>18</sup> Then the surface was annealed step-by-step to increasing temperatures (10 min/annealing cycle), resulting in preferential desorption of molecules with lower binding energies. Analyzing the CO coverage as a function of temperature provides the CO adsorption energies, which can be compared to the TPD results. STM also reveals potential adsorption sites with higher CO binding energy and allow us to estimate CO–CO interactions (see below).

Figure 3 shows an example of STM images obtained in this way. Figure 3a shows 1 ML coverage; other panels show the surface after annealing to increasing temperatures. We note that isolated CO molecules appear twinned (Figure 3c) because of their “wagging” motion.<sup>14</sup> Figure 4 shows the CO coverage as a function of the annealing temperature. The experiment was repeated on two different samples (different symbols in Figure 4; sample 2 was identical to the one used for the TPD experiments). The samples were subjected to varying numbers of sputter–anneal cycles, ranging from a few up to hundreds of cycles. The CO desorption shows only subtle variations with the specific sample used or its pretreatment.

We model the data in Figure 4 assuming again first-order desorption. The annealing cycles were approximated by keeping the sample at the corresponding temperature for 200 s (assuming first 400 s for thermal equilibration). The same frequency prefactor as for the TPD analysis was used,  $v_0 = 10^{13} \text{ s}^{-1}$ , and the adsorption energy,  $E_{\text{ads}}$ , was treated as a parameter. The data can be reasonably well fitted by a single adsorption energy of  $E_{\text{ads}1} = 0.34 \text{ eV}$ , with a shoulder corresponding to an  $E_{\text{ads}2}$  of 0.38 eV. The height of the shoulder seems to be dependent on the particular sample; we observed a correlation with the concentration of the defects marked in Figure 3d, which are characteristic for the anatase (101) surface, and previously they were attributed to extrinsic donors.<sup>38</sup>

A careful analysis of the STM images shows that this shoulder corresponds to CO molecules adsorbed in the vicinity of these subsurface donors, see Figure 3c. The surrounding of the donors appears bright in STM images<sup>39</sup> because of the surplus of excess electrons. The preference for occupying these bright regions indicates slightly stronger CO bonding in the vicinity of these donors. The shoulder observed in STM

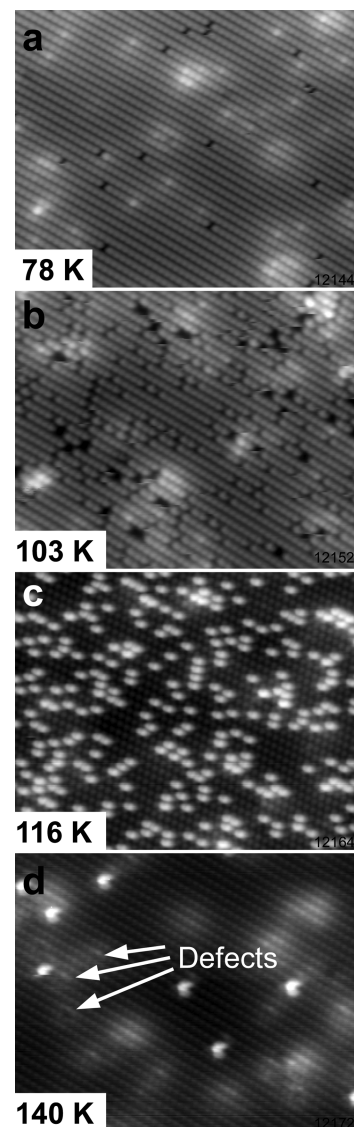


**Figure 3.** Effects of heating on CO adsorbed on anatase (101), monitored with STM. A full monolayer of CO was dosed at  $T = 78 \text{ K}$ , and the surface was annealed to increasing temperatures in  $\sim 5 \text{ K}$  steps. Panels a–d show representative STM images after annealing for 10 min to the indicated temperatures ( $20 \times 16 \text{ nm}^2$  each;  $V_S = +1.0 \text{ V}$ ;  $I_T = 0.1 \text{ nA}$ ). Marked in panel d are defects (likely subsurface impurities), where the CO desorption temperature is highest.

measurements (Figure 4) is attributed to the same physical mechanism as the enhancement in the binding energies extracted from the TPD measurements (Figure 2b) at low coverages.

**XPS.** We also took XPS spectra for various CO coverages, see Figure 5. The C 1s peak is found at 290.5 eV for 0.4 langmuir and shifts up to 291 eV at 2.8 langmuir. The CO-related peak in the O 1s state is found at 536.8 eV for 0.4 langmuir dose and shifts to 537.2 eV at 2.8 langmuir. These values are consistent with the ones obtained for weakly adsorbed CO on noble metal surfaces<sup>40,41</sup> and with the C 1s binding energy reported for  $\text{CO}/\text{Co}_2\text{O}_3$ .<sup>42</sup> We checked for beam damage of the sample by measuring TPD spectra immediately after the XPS acquisition; they were identical to the ones for the nonirradiated sample.

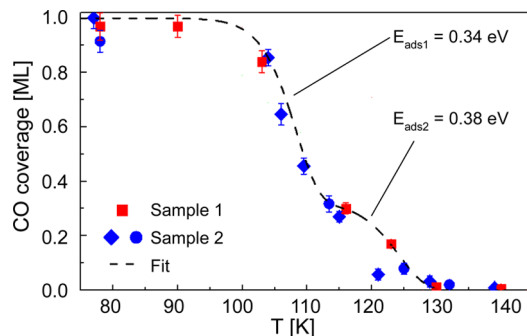


**Figure 4.** CO coverage on anatase (101) as a function of annealing temperature. Red symbols denote data measured on the sample corresponding to STM images shown in Figure 3. Blue symbols correspond to the sample used for TPD in Figure 2. The dashed line is a fit of the data based on first-order desorption with  $\nu = 10^{13} \text{ s}^{-1}$  and using two adsorption energies of 0.34 and 0.38 eV, weighted in ~2:1 ratio.

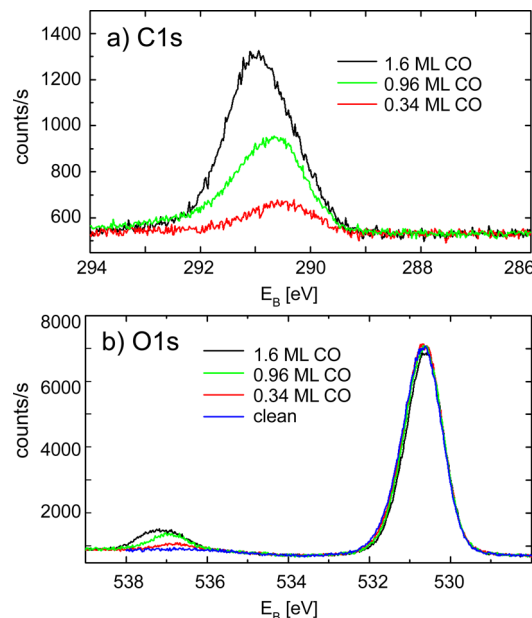


**Figure 5.** XPS spectra for different doses of CO adsorbed on the anatase (101) surface taken with monochromatized Al K $\alpha$  radiation at  $T = 34 \text{ K}$ : (a) C 1s region and (b) O 1s region.

**DFT Calculations.** In our DFT calculations, we described the sample reduction with two different models, either including a subsurface oxygen vacancy (located in the second layer below the surface, see Figure 6) or adding two hydrogen atoms to the backside of the slab. The calculated adsorption energies and CO stretching frequencies are listed in Table 1. Here,  $\Delta\nu$  represents the calculated frequency shift relative to the computed stretching frequency of gas-phase CO, and  $\nu$  (corrected) is obtained by adding this  $\Delta\nu$  to the experimental CO gas-phase stretching frequency of  $2143 \text{ cm}^{-1}$ . The computed gas-phase CO frequencies by linear response and finite differences are  $2149$  and  $2110 \text{ cm}^{-1}$ , respectively.

For stoichiometric anatase (101) the calculations yield an adsorption energy of  $0.26 \text{ eV}$  for a single adsorbed CO molecule.  $E_{\text{ads}}$  slightly decreases with increasing coverage, which is accompanied by a red-shift in the vibrational frequency. Similar CO coverage effects have been reported in ref 21. The calculated coverage-related decrease in the adsorption energies

shows a good agreement with the experimental data. The measured coverage-dependent frequency shift of  $\sim 4 \text{ cm}^{-1}$  is close to the detection limit, less than the calculated  $10 \text{ cm}^{-1}$ .

As typical for the PBE functional, the adsorption energies are underestimated because dispersion (van der Waals (vdW)) interactions are not included. However, inclusion of simple vdW correction terms<sup>43</sup> to PBE overestimates the adsorption energy (see Table 1). Nonetheless, the stretching frequencies in Table 1 are similar to the experimental values, indicating that the calculations describe the CO frequency shifts well.

The calculation for a reduced surface with a subsurface  $V_O$  shows an enhanced electron density above the  $V_O$ .<sup>44</sup> CO strongly prefers adsorption above the  $V_O$  (site 7 in Figure 6b); there, CO adsorption is 60% stronger than at the stoichiometric surface. This is accompanied by a significant redshift of the CO stretching frequency by approximately  $30 \text{ cm}^{-1}$ . Other adsorption positions yield binding energies and stretching frequencies comparable to a stoichiometric surface (see Table 1). In the surface model reduced by the hydrogen atoms at the backside of the slab, the excess electrons are delocalized, causing only a minor enhancement of the electron density in the surface regime.<sup>45</sup> As a consequence, the CO adsorption energies slightly increase compared to the stoichiometric surface, yet there is no strongly preferred adsorption position. Also, the calculated redshift is lower,  $\sim 7 \text{ cm}^{-1}$ .

## DISCUSSION

**Bonding of CO.** The CO bonding to different surfaces has historically attracted much attention.<sup>37,46–50</sup> The interaction between CO and oxide surfaces has been reviewed in ref 37, and the specific case of CO adsorption on TiO<sub>2</sub> has been considered in several ab initio studies, e.g., in refs 27, 48, and 51. The main contribution to the bonding energy arises from electron donation from the carbon 5 $\sigma$  orbital to the Ti–C  $\sigma$ -bond. The electrostatic effect often plays a major role in bonding to cations on oxides,<sup>37</sup> it is almost entirely canceled by the Pauli repulsion in TiO<sub>2</sub>.<sup>48,51</sup> The stretching mode of a CO molecule adsorbed on stoichiometric TiO<sub>2</sub> is blue-shifted with respect to the gas phase ( $2143 \text{ cm}^{-1}$ ), mainly because of the electrostatic polarization of the CO dipole by the metal cation (Stark effect) and Pauli repulsion occurring when the molecule vibrates against a rigid surface (wall effect).<sup>51</sup>

A possible backdonation to antibonding  $\pi^*$  orbitals of the CO molecule would increase the binding energy and cause a redshift in the CO stretching frequency. All adsorption sites on anatase (101) are equivalent from the structural point of view. Thus, CO acts as a sensitive probe for excess electrons in the material; the excess electrons within the bandgap of TiO<sub>2</sub> have suitable energies for the backdonation. The differential electron density for the three types of slab considered in this work is shown in Figure 6c–e. The corresponding PDOS is shown in Figure 7.

When the anatase (101) surface is reduced by including subsurface oxygen vacancies, the calculated adsorption energy and stretching frequency above the  $V_O$  show a distinct difference compared to other adsorption positions at the surface, see Table 1 and Figure 6. The vibrational frequency becomes red-shifted by  $30 \text{ cm}^{-1}$ . While an O-vacancy-induced shift was experimentally observed for rutile TiO<sub>2</sub>(110) and CeO<sub>2</sub>(111) surfaces ( $\sim 10 \text{ cm}^{-1}$ ),<sup>47,48</sup> this effect is absent in reduced anatase. At the position directly above the vacancy the binding energy is predicted to increase by  $0.15 \text{ eV}$  as compared to sites that are not affected by the  $V_O$ . While STM shows that

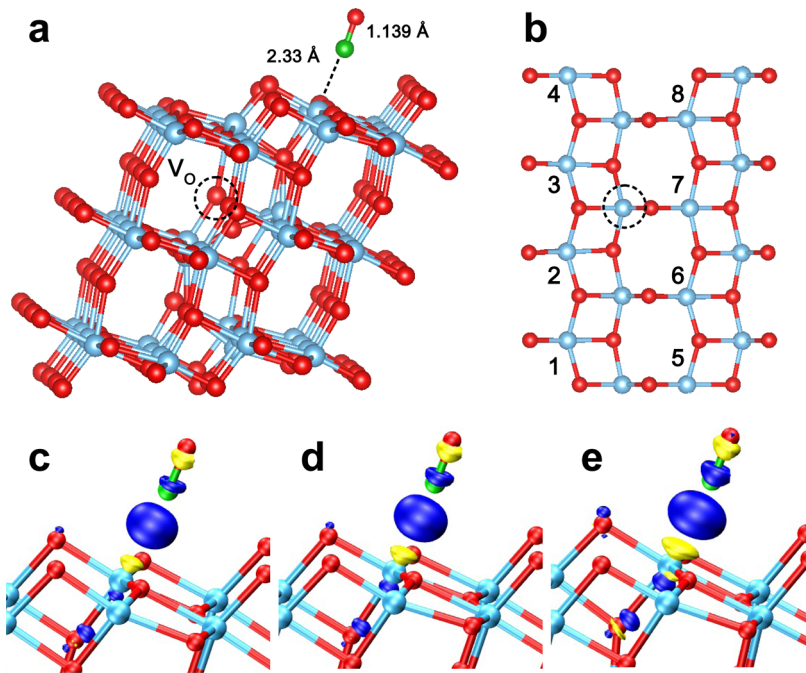


**Figure 6.** Calculated CO adsorption configuration on the anatase (101) surface. (a) A slab with a subsurface oxygen vacancy. (b) Top view of the slab. The dashed circle marks the position of the subsurface  $V_O$ , and numbers mark different adsorption positions. Panels c–e show CO on (c) a stoichiometric slab, (d) a slab with two H atoms on the back side, and (e) position 7 of the slab with a subsurface  $V_O$ . Blue and yellow isosurfaces indicate increase and decrease ( $\pm 0.004$  a.u) of the electron density, respectively, with respect to the sum of the charge densities of the slab and molecule.

**Table 1. Summary of the DFT-PBE Results of CO Adsorption on Anatase (101)<sup>a</sup>**

	CO coverage [ML]	$E_{ads}$ [eV]	$\Delta\nu$ calculated [ $\text{cm}^{-1}$ ]	$\nu$ (corrected) [ $\text{cm}^{-1}$ ]	method
anatase stoichiometric	0.125	0.262	39.3	2182	finite differences
	1	0.221	30	2173	
anatase stoichiometric	0.25	0.255 (0.461)	39	2182	linear response
	1	0.213	29	2172	
anatase reduced $V_O$	0.125 ( $V_O$ )	0.420	6.8	2150	finite differences
	0.125 (other)	0.22–0.27	32.7–35.7	2176–2179	
anatase reduced 2×H	0.25 (pos1)	0.270	31.6	2175	linear response
	0.25 (pos4)	0.282 (0.531)	36.8	2180	

<sup>a</sup>Results including Grimme D2 dispersion corrections<sup>33</sup> are in parentheses. The two values for reduced anatase refer to inequivalent adsorption sites relative to the reducing defect, e.g.,  $V_O$  corresponds to the geometry shown in Figure 6a with CO adsorbed above the subsurface vacancy (site 7 in Figure 6b).

some molecules do adsorb more strongly than others, the measured difference in binding (0.04 eV) energy is far smaller than this value. From both the TPD and STM measurements, we can say that the number of CO molecules significantly exceeding the regular adsorption energy by more than 0.1 eV is less than 0.01 ML. We conclude that the oxygen vacancies created by the sputter-anneal process are not located in the second layer (as in our reduced surface model in Figure 6a). They must be located deeper.

Among the two DFT models for the reduced surface in this study, the slab model with H atoms on the backside provides the closest match to the experimental data. The difference between the H-reduced and  $V_O$ -reduced slabs lies in the distribution of the excess electrons. A subsurface  $V_O$  forms a defect in the crystal lattice, which results in an enhancement of the electron density above the  $V_O$ . The localized excess charge above the subsurface  $V_O$  would lead to enhanced backdonation into the CO antibonding orbitals, a strong increase of the CO binding energy, and a redshift of the CO stretching frequency;

these effects are not observed experimentally. Our results are consistent with electrons that are delocalized throughout the anatase lattice.<sup>45</sup>

**CO–CO Interactions.** Both the binding energy and the vibrational frequency can be affected by CO–CO interactions. Our DFT calculations predict a significant redshift of 10  $\text{cm}^{-1}$  in the CO stretching frequency from 0.25 to 1 ML coverage on the stoichiometric surface. The experimental data, however, show a shift of only 3  $\text{cm}^{-1}$  for the corresponding coverages. Another mechanism affecting the adsorption energy is the repulsive interaction between CO molecules related to their dipole moments. Our DFT results predict that this shift should be rather small (on the order of 0.04 eV). This is consistent with the TPD results in Figure 2b, which show a small decrease of the binding energy with coverage. Interestingly, this shift is much smaller than in rutile, where  $E_{des}$  was found to decrease to half its value when going from the isolated molecule to monolayer coverage.<sup>18,19</sup> This was attributed to a strong CO–CO repulsion; apparently the effect is much smaller on anatase

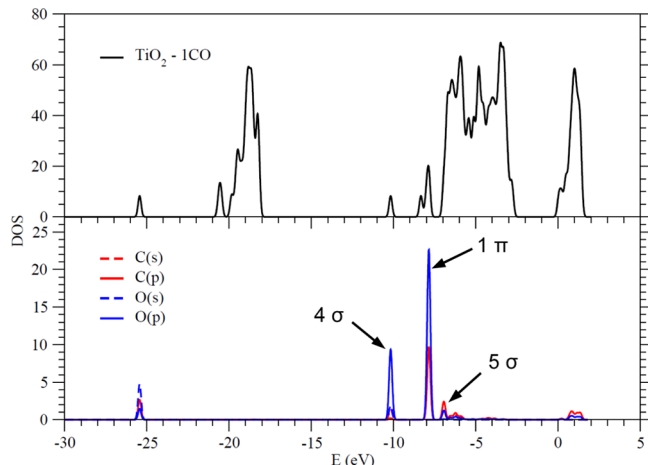


**Figure 7.** Density of states (DOS) of a CO molecule adsorbed on a  $\text{TiO}_2$  slab reduced by two adsorbed hydrogen atoms. The top panel shows the total DOS; the lower panel shows the DOS projected on the CO molecule. The main orbital contribution to the peaks in the CO-projected DOS is indicated.

(101) than rutile (110), possibly also because of the larger intermolecular distances in the former case.

The CO–CO repulsive energy can be estimated by analyzing STM data. Annealing the CO monolayer to a well-defined temperature brings the system close to a state where we can assume that the probabilities of occupying adsorption sites with different energies are in equilibrium, i.e., their position should follow the Boltzmann distribution. Thus, the repulsive interaction energies between two CO molecules can be directly determined from an autocorrelation function of CO positions

$$E_{\text{rep}} = -kT \ln \left( \frac{p(\text{nearest neighbor})}{p(\text{average})} \right) \quad (2)$$

where  $p$  denotes the value of the autocorrelation function at a given point. This equation is valid for low coverages, where the average distances between two molecules (in a given direction) are smaller than the characteristic radius of the repulsive interaction. An example of such an autocorrelation function is shown in Figure 8. The following procedure was used to calculate the autocorrelation function: The STM image was first undistorted in order to remove any effects of piezo creep.<sup>52</sup> Then the positions of the CO molecules were determined by an automatic feature-recognition procedure and corrected manually when necessary. The autocorrelation was calculated from the resulting function and was discretized to the surface unit cells. Analysis by means of eq 2 provides the nearest-neighbor repulsive interaction of only 3.4 meV, consistent with the small decrease in adsorption energy shown in Figure 2b. We note that the identical procedure performed on rutile provides a ~10 times higher repulsive energy.

**Comparison to Rutile.** The data in Figure 8 confirm that the repulsive CO–CO interactions in the CO layer adsorbed on anatase (101) are rather small. The TPD peak broadening consists of two contributions: The adsorption energies are enhanced at low coverages because of the electron backdonation. At high coverages, the adsorption energies are slightly lowered because of the CO–CO repulsive interactions in the layer. The smaller shift in peak position with coverage compared to rutile likely originates from the difference in the behavior of excess electrons. Excess electrons in rutile always

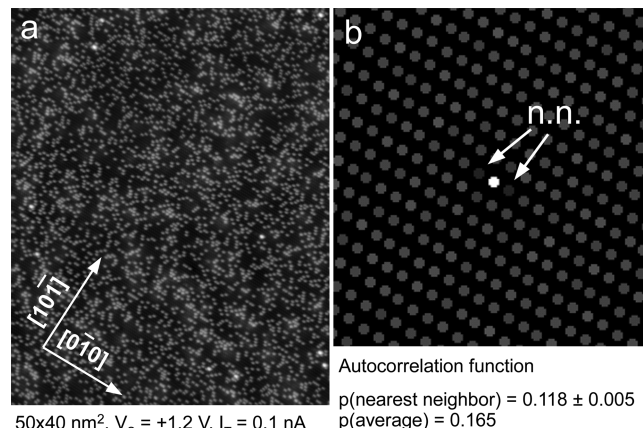


**Figure 8.** (a) Anatase (101) surface after dosing 1 ML of CO and subsequent annealing to 123 K for 10 min. (b) Grayscale map of the autocorrelation function of CO positions obtained from analysis of panel a. Disks darker than average indicate low autocorrelation, i.e., repulsion.

form localized polarons,<sup>45</sup> regardless of how they are donated to the lattice. Likely this is the reason for forming two distinct CO adsorption configurations on the rutile (110) surface.<sup>17,20</sup> CO molecules coupled and not-coupled to a polaron. In contrast, differences between CO molecules are significantly weaker on anatase (101). Anatase shows only one pronounced peak in the infrared spectra, and the adsorption energies of all CO molecules are rather similar. We attribute this to the lack of electron localization in anatase.<sup>45</sup>

## CONCLUSIONS

In summary, CO adsorption on anatase  $\text{TiO}_2(101)$  shows a simple behavior. The measured adsorption energy for zero-coverage limit is  $0.37 \pm 0.03$  eV. The adsorption energy in the vicinity of subsurface donors increases by up to 40 meV, which we attribute to the electron backdonation. Upon increasing coverage, the CO adsorption energy is weakened because of dipole–dipole repulsive interactions, but these are small. The CO stretch frequency is  $\sim 2181 \text{ cm}^{-1}$ , independent of the reduction state. In contrast to rutile  $\text{TiO}_2(110)$ , no additional CO vibrational peaks or strongly bound CO species are seen for the reduced substrate. We attributed the observed behavior to the lack of O-vacancy-induced small polarons in anatase and its preference for delocalized electrons. Our data also indicate that single subsurface oxygen vacancies directly below the anatase (101) surface (i.e., in the second layer) must be a rather rare species. Comparison between computational and experimental results indicates that adding delocalized electrons, e.g., through adsorbed hydrogen atoms on the backside of the slab, provides a suitable model of reduced anatase for DFT calculations.

## AUTHOR INFORMATION

### Corresponding Author

\*E-mail: setvin@iap.tuwien.ac.at

### Notes

The authors declare no competing financial interest.

## ACKNOWLEDGMENTS

The work was supported by the ERC Advanced Grant “OxideSurfaces”. A.S. and W.H. acknowledge the support of

DoE-BES, Division of Chemical Sciences, Geosciences and Biosciences under Award DE-FG02-12ER16286. M.B. has been supported through the Helmholtz Research School "Energy-related catalysis".

## ■ REFERENCES

- (1) Linsebigler, A.; Lu, G.; Yates, J. T. Photocatalysis on TiO<sub>2</sub> surfaces: Principles, Mechanisms and Selected Results. *Chem. Rev.* **1995**, *95*, 735–758.
- (2) Fujishima, A.; Honda, K. Electrochemical Photolysis of Water at a Semiconductor Electrode. *Nature* **1972**, *238* (5358), 37–38.
- (3) Thompson, T. L.; Yates, J. T. Surface Science Studies of the Photoactivation of TiO<sub>2</sub> - New Photochemical Processes. *Chem. Rev.* **2006**, *106*, 4428–4453.
- (4) Grätzel, M. Photoelectrochemical Cells. *Nature* **2001**, *414*, 338–344.
- (5) Furubayashi, Y.; Hitosugi, T.; Yamamoto, Y.; Inaba, K.; Kinoda, G.; Hirose, Y.; Shimada, T.; Hasegawa, T. A Transparent Metal: Nb-doped Anatase TiO<sub>2</sub>. *Appl. Phys. Lett.* **2005**, *86*, 252101.
- (6) Moser, S.; Moreschini, L.; Jacimovic, J.; Baršić, O. S.; Berger, H.; Magrez, A.; Chang, Y. J.; Kim, K. S.; Bostwick, A.; Rotenberg, et al. M. Tunable Polaronic Conduction in Anatase TiO<sub>2</sub>. *Phys. Rev. Lett.* **2013**, *110*, 196403.
- (7) Szot, K.; Rogala, M.; Speier, W.; Klusek, Z.; Besmehn, A.; Waser, R. TiO<sub>2</sub> — A Prototypical Memristive Material. *Nanotechnology* **2011**, *22*, 254001.
- (8) Diebold, U. The Surface Science of Titanium Dioxide. *Surf. Sci. Rep.* **2003**, *48*, 53–229.
- (9) Green, I. X.; Tang, W.; Neurock, M.; Yates, J. T. Spectroscopic Observation of Dual Catalytic Sites During Oxidation of CO on a Au/TiO<sub>2</sub> Catalyst. *Science* **2011**, *333*, 736–739.
- (10) Vannice, M. A. Titania-Supported Metals as CO Hydrogenation Catalysts. *J. Catal.* **1982**, *74*, 199–202.
- (11) Sato, Y.; Koizumi, M.; Miyao, T.; Naito, S. The CO–H<sub>2</sub> and CO–H<sub>2</sub>O Reactions Over TiO<sub>2</sub> Nanotubes Filled with Pt Metal Nanoparticles. *Catal. Today* **2006**, *111*, 164–170.
- (12) Bocuzzi, F.; Guglielminotti, E.; Martra, G.; Cerrato, G. Nitric Oxide Reduction by CO on Cu/TiO<sub>2</sub> Catalysts. *J. Catal.* **1994**, *146*, 449–459.
- (13) Cotton, F. A.; Wilkinson, G.; Murillo, C. A. *Advanced Inorganic Chemistry*; Wiley-Interscience: New York, 1999.
- (14) Setvin, M.; Daniel, B.; Aschauer, U.; Hou, W.; Li, Y.-F.; Schmid, M.; Selloni, A.; Diebold, U. Identification of Adsorbed Molecules via STM Tip Manipulation: CO, H<sub>2</sub>O, and O<sub>2</sub> on TiO<sub>2</sub> Anatase (101). *Phys. Chem. Chem. Phys.* **2014**, *16*, 21524–21530.
- (15) Zhao, Y.; Wang, Z.; Cui, Y.; Huang, T.; Wang, B.; Luo, Y.; Yang, J.; Hou, J. What Are the Adsorption Sites for CO on the Reduced TiO<sub>2</sub>(110)-1 × 1 Surface? *J. Am. Chem. Soc.* **2009**, *131*, 7958–7959.
- (16) Miessler, G. L.; Tarr, D. A. *Inorganic Chemistry*. Prentice Hall: Upper Saddle River, NJ, 1999.
- (17) Kunat, M.; Traeger, F.; Silber, D.; Qiu, H.; Wang, Y.; van Veen, A. C.; Wöll, C.; Kowalski, P. M.; Meyer, B.; Hättig, C.; Marx, D. Formation of Weakly Bound, Ordered Adlayers of CO on Rutile TiO<sub>2</sub>(110): A Combined Experimental and Theoretical Study. *J. Chem. Phys.* **2009**, *130*, 144703.
- (18) Dohnalek, Z.; Kim, J.; Bondarchuk, O.; White, J. M.; Kay, B. D. Physisorption of N<sub>2</sub>, O<sub>2</sub>, and CO on Fully Oxidized TiO<sub>2</sub>(110). *J. Phys. Chem. B* **2006**, *110*, 6229–6235.
- (19) Petrik, N. G.; Kimmel, G. A. Adsorption Geometry of CO versus Coverage on TiO<sub>2</sub>(110) from sand p-Polarized Infrared Spectroscopy. *J. Phys. Chem. Lett.* **2012**, *3*, 3425–3430.
- (20) Xu, M.; Noei, H.; Fink, K.; Muhler, M.; Wang, Y.; Wöll, C. The Surface Science Approach for Understanding Reactions on Oxide Powders: The Importance of IR Spectroscopy. *Angew. Chem., Int. Ed.* **2012**, *51*, 4731–4734.
- (21) Mino, L.; Ferrari, A. M.; Lacivita, V.; Spoto, G.; Bordiga, S.; Zecchina, A. CO Adsorption on Anatase Nanocrystals: A Combined Experimental and Periodic DFT Study. *J. Phys. Chem. C* **2011**, *115*, 7694–7700.
- (22) Mino, L.; Spoto, G.; Bordiga, S.; Zecchina, A. Particles Morphology and Surface Properties As Investigated by HRTEM, FTIR, and Periodic DFT Calculations: From Pyrogenic TiO<sub>2</sub> (P2S) to Nanoanatase. *J. Phys. Chem. C* **2012**, *116*, 17008–17018.
- (23) Mino, L.; Spoto, G.; Bordiga, S.; Zecchina, A. Rutile Surface Properties Beyond the Single Crystal Approach: New Insights from the Experimental Investigation of Different Polycrystalline Samples and Periodic DFT Calculations. *J. Phys. Chem. C* **2013**, *117*, 11186–11196.
- (24) Xu, M.; Gao, Y.; Moreno, E.; Kunst, M.; Muhler, M.; Wang, Y.; Idriss, H.; Wöll, C. Photocatalytic Activity of Bulk TiO<sub>2</sub> Anatase and Rutile Single Crystals Using Infrared Absorption Spectroscopy. *Phys. Rev. Lett.* **2011**, *106*, 138302.
- (25) He, Y.; Dulub, O.; Cheng, H.; Selloni, A.; Diebold, U. Evidence for the Predominance of Subsurface Defects on Reduced Anatase TiO<sub>2</sub>(101). *Phys. Rev. Lett.* **2009**, *102*, 106105.
- (26) Scheiber, P.; Fidler, M.; Dulub, O.; Schmid, M.; Diebold, U.; Hou, W.; Aschauer, U.; Selloni, A. (Sub)Surface Mobility of Oxygen Vacancies at the TiO<sub>2</sub> Anatase (101) Surface. *Phys. Rev. Lett.* **2012**, *109*, 136103.
- (27) Lustemberg, P. G.; Scherlis, D. A. Monoxide Carbon Frequency Shift as a Tool for the Characterization of TiO<sub>2</sub> Surfaces: Insights From First Principles Spectroscopy. *J. Chem. Phys.* **2013**, *138*, 124702.
- (28) Setvin, M.; Daniel, B.; Mansfeldova, V.; Kavan, L.; Scheiber, P.; Fidler, M.; Schmid, M.; Diebold, U. Surface Preparation of TiO<sub>2</sub> Anatase (101): Pitfalls and How to Avoid Them. *Surf. Sci.* **2014**, *626*, 61–67.
- (29) Buchholz, M.; Weidler, P. G.; Bebensee, F.; Nefedov, A.; Wöll, C. Carbon Dioxide Adsorption on a ZnO(10–10) Substrate Studied by Infrared Reflection Absorption Spectroscopy. *Phys. Chem. Chem. Phys.* **2014**, *16*, 1672–1678.
- (30) Giannozzi, P.; Baroni, S.; Bonini, N.; Calandra, M.; Car, R.; Cavazzoni, C.; Ceresoli, D.; Chiarotti, G. L.; Cococcioni, M.; Daboli, I.; et al. Quantum Espresso: A Modular and Open-Source Software Project for Quantum Simulations of Materials. *J. Phys.: Condens. Matter* **2009**, *21*, 395502.
- (31) Aschauer, U.; He, Y.; Cheng, H.; Li, S.-C.; Diebold, U.; Selloni, A. Influence of Subsurface Defects on the Surface Reactivity of TiO<sub>2</sub>: Water on Anatase (101). *J. Phys. Chem. C* **2010**, *114*, 1278–1284.
- (32) Aschauer, U.; Chen, J.; Selloni, A. Peroxide and Superoxide States of Adsorbed O<sub>2</sub> on Anatase TiO<sub>2</sub> (101) with Subsurface Defects. *Phys. Chem. Chem. Phys.* **2010**, *12*, 12956–12960.
- (33) Grimme, S. Semiempirical GGA-type Density Functional Constructed With a Long-Range Dispersion Correction. *J. Comput. Chem.* **2006**, *27*, 1787–1799.
- (34) Vanderbilt, D. Soft Self-Consistent Pseudopotentials In A Generalized Eigenvalue Formalism. *Phys. Rev. B: Condens. Matter Mater. Phys.* **1990**, *41*, 7892–7895.
- (35) Yang, C.; Yin, L.-L.; Bebensee, F.; Buchholz, M.; Sezen, H.; Heissler, S.; Chen, J.; Nefedov, A.; Idriss, H.; Gong, X.-Q.; Wöll, C. Chemical Activity of Oxygen Vacancies on Ceria: A Combined Experimental and Theoretical Study on CeO<sub>2</sub>(111). *Phys. Chem. Chem. Phys.* **2014**, *16*, 24165–24168.
- (36) Dohnalek, Z.; Kimmel, G. A.; Joyce, S. A.; Ayotte, P.; Smith, R. S.; Kay, B. D. Physisorption of CO on the MgO(100) Surface. *J. Phys. Chem. B* **2001**, *105*, 3747–3751.
- (37) Hadjiivanov, K. I.; Vayssilov, G. N. Characterization of Oxide Surfaces and Zeolites by Carbon Monoxide as an IR Probe Molecule. *Adv. Catal.* **2002**, *47*, 307–511.
- (38) Setvin, M.; Aschauer, U.; Scheiber, P.; Li, Y. F.; Hou, W.; Schmid, M.; selloni, A.; Diebold, U. Reaction of O<sub>2</sub> with Subsurface Oxygen Vacancies on TiO<sub>2</sub> Anatase (101). *Science* **2013**, *341*, 988–991.
- (39) Ebert, P. Nano-scale Properties of Defects in Compound Semiconductor Surfaces. *Surf. Sci. Rep.* **1999**, *33*, 121–303.

- (40) Norton, P. R.; Tapping, R. L.; Goodale, J. W. High Resolution Photoemission Study of the Physisorption and Chemisorption of CO on Copper and Gold. *Surf. Sci.* **1978**, *72*, 33–44.
- (41) Freund, H. J.; Plummer, E. W. Explanation of the Satellite Structure Observed in the Photoemission Spectra of Coordinated CO. *Phys. Rev. B: Condens. Matter Mater. Phys.* **1981**, *23*, 4859–4878.
- (42) Kuhlenbeck, H.; Xu, C.; Dillmann, B.; Hassel, M.; Adam, B.; Ehrlich, D.; Wohlrab, S.; Freund, H. J.; Ditzinger, U. A.; Neddermeyer, H.; Neuber, M.; et al. Adsorption and Reaction of Molecules on Surfaces of Metal–Metal Oxide Systems. *Ber. Bunsenges. Phys. Chem.* **1992**, *96*, 15–27.
- (43) Grimme, S.; Antony, J.; Ehrlich, S.; Krieg, H. A Consistent and Accurate ab initio Parametrization of Density Functional Dispersion Correction (DFT-D) for the 94 Elements H–Pu. *J. Chem. Phys.* **2010**, *132*, 154104.
- (44) Cheng, H. Z.; Selloni, A. Energetics and Diffusion of Intrinsic Surface and Subsurface Defects on Anatase TiO<sub>2</sub>(101). *J. Chem. Phys.* **2009**, *131*, 054703.
- (45) Setvin, M.; Franchini, C.; Hao, X.; Schmid, M.; Janotti, A.; Kaltak, M.; Van de Walle, C. G.; Kresse, G.; Diebold, U. A Direct View at Excess Electrons in TiO<sub>2</sub> Rutile and Anatase. *Phys. Rev. Lett.* **2014**, *113*, 086402.
- (46) Miessler, G. L.; Tarr, D. A. *Inorganic Chemistry*; Springer-Verlag: New York, 1999.
- (47) Blyholder, G. Molecular Orbital View of Chemisorbed Carbon Monoxide. *J. Phys. Chem.* **1964**, *68*, 2772–2777.
- (48) Casarin, M.; Maccato, C.; Vittadini, A. Molecular Chemisorption on TiO<sub>2</sub>(110): A Local Point of View. *J. Phys. Chem. B* **1998**, *102*, 10745–10752.
- (49) Föhlisch, A.; Nyberg, M.; Bennich, P.; Triguero, L.; Hasselström, J.; Karis, O.; Pettersson, L. G. M.; Nilsson, A. The Bonding of CO to Metal Surfaces. *J. Chem. Phys.* **2000**, *112*, 1946–1958.
- (50) Föhlisch, A.; Nyberg, M.; Hasselström, J.; Karis, O.; Pettersson, L. G. M.; Nilsson, A. How Carbon Monoxide Adsorbs in Different Sites. *Phys. Rev. Lett.* **2000**, *85*, 3309–3312.
- (51) Pacchioni, G.; Cogliandro, G.; Bagus, P. S. Characterization of Oxide Surfaces by Infrared Spectroscopy of Adsorbed Carbon Monoxide: A Theoretical Investigation of the Frequency Shift of CO on MgO and NiO. *Surf. Sci.* **1991**, *255*, 344–354.
- (52) Choi, J. I. J.; Mayr-Schmöller, W.; Mittendorfer, F.; Redinger, J.; Diebold, U.; Schmid, M. The Growth of Ultra-Thin Zirconia Films on Pd<sub>3</sub>Zr(0001). *J. Phys.: Condens. Matter* **2014**, *26*, 225003.